Flow Turbulence Combust (2011) 87:1–31
DOI 10.1007/s10494-011-9325-4

On the Vortex Dynamic of Airflow Reattachment Forced by a Single Non-thermal Plasma Discharge Actuator

Nicolas Benard · Eric Moreau

Received: 17 July 2010 / Accepted: 15 January 2011 / Published online: 17 February 2011
© Springer Science+Business Media B.V. 2011

Abstract Commercial and military aircrafts or miniature aerial vehicles can suffer from massive flow separation when high angles of attack are required. Single dielectric barrier discharge (DBD) actuators have demonstrated their capability of controlling such a separated flow at low external velocity. However, the processes resulting in the improvement of the flight performances remain unclear. In the present study, the reattachment process along the suction side of a NACA 0015 placed at an angle of attack of 16° is experimentally investigated for an external velocity of 20 m/s (Re = 260,000). A single DBD actuator is mounted at the leading edge of the model. The velocity fields above the suction side of the airfoil are measured by a high-speed acquisition system (3 kHz). The results indicate that the baseline flow presents shed vortices that form at the leading edge and linearly grow along the free shear layer axis. This vortex shedding is organized and exhibits a specific frequency of about 90 Hz. The continuous actuation produces a partial flow reattachment up to 70% of the chord length. Temporal cross-correlation function indicates the presence of a vortex shedding at the trailing edge of the controlled flow. Finally, the temporal analysis demonstrates that the reattachment process requires 50 ms to reach a stabilized attached flow. The time-resolved analysis of the reattachment suggests that the actuation by plasma discharge acts as a catalyser by reinforcing one of the coherent flow structures already existing in the natural flow.

Keywords Flow control · Plasma actuator · Dielectric barrier discharge · Separated airflow · Vortex dynamics

N. Benard (✉) · E. Moreau
Dpt Fluides, Thermique, Combustion, Institut Pprime
(CNRS – University of Poitiers – ENSMA),
SP2MI – Teleport 2, Bld Marie et Pierre Curie,
BP 30179, 86962 Futuroscope, France
e-mail: nicolas.benard@univ-poitiers.fr

1 Introduction

Flow separation usually occurs due to the viscous effects, an adverse pressure gradient or a geometric accident. Such flow separation over the suction side of an airfoil results in a drastic lift decrease and drag increase. Civil and military aircrafts prevent the flow separation at high angle of attack by adding a mechanical system at the leading and trailing edges. Flat and slat are efficient mechanical system that can delay stall and increase lift, but the technical complexity, the radiated noise and the additional weight of these systems may restrict their implementation on Miniature Aerial Vehicles (MAVs). These type of small scale aircrafts operate at low flight Reynolds number (typically lower than 10^5) and they can also experience massive flow separation. The low speed of these aircrafts supports the investigation of active control device that can be easily implemented without significant mass penalty.

Non-thermal plasma actuators are effective devices to control the flow separation occurring over aerodynamic surfaces at high incidence and low speed conditions [1, 2]. Previous experimental studies about flow separation controlled by non-thermal plasma actuation have demonstrated that the stall regime can be delayed for NACA 0012 [3], NACA 0015 [4–6] or other airfoils profiles [7, 8] (Reynolds number up to 4×10^5). Plasma actuators are attractive for aerospace and MAVs applications because they are simple, lightweight and constitute low-cost devices. In particular actuators based on Dielectric Barrier Discharge (DBD) are only made of two thin electrodes asymmetrically flush mounted on a dielectric material. The local flow produced by such an actuator results from the formation of a plasma discharge over the dielectric wall by supplying a high-voltage to one of the electrode. In 1998, Roth has demonstrated that a local flow useful for flow manipulation can be produced in the plasma region, tangentially to the dielectric wall surface [9]. Different authors have investigated the mechanism of the local airflow formation [10–12]. Charged particles (ions and electrons) are produced in the inter electrode space due to the electric field. A momentum transfer from the charged particles to the neutral atmospheric air components produces a local flow of a few m/s usually called 'ionic wind' or 'electric wind' [10–12]. Further investigations have been conducted in order to optimize the electrode geometry resulting in the improvement of the 'electric wind' produced by a single DBD actuator. Currently, the flow velocity produced by the electromechanical conversion rarely exceeds 7 m/s [13, 14]. Studies have also demonstrated the capability of a DBD actuator to be operated at high altitude or high humidity conditions that approach real atmospheric flight conditions [15, 16]. Each new publication related to DBD actuators tends to demonstrate that these devices can compete with others active control systems such as blowing jets, synthetic jets or piezoelectric.

Dielectric barrier discharge actuators are used to transfer momentum into the boundary layer of flows with moderate Reynolds number. A DBD actuator is characterized by a momentum transferred from the outer part of the flow (above the electrode) to the parietal region without mass flow addition due to the control system. In fact, it acts as a local force on the fluid. This property has been extensively used to promote and maintain partial and full airflow reattachment along airfoil profiles. However, the mechanisms responsible for the reattachment are still unclear since most of the literature focused on global force measurements, time-averaged velocity fields or measurements of the mean pressure distribution at the airfoil

surfaces. The time-resolved effects of the control on the surrounding flow remain to be investigated. In particular, the resultant of the interactions between the ionized airflow produced by the single DBD actuator and the overall flow structures remains to be experimentally observed and qualified.

In the present study the flow over a NACA 0015 in post-stall regime ($\alpha = 16°$) is experimentally investigated. A single DBD actuator is mounted at the leading edge of an airfoil placed in an open wind tunnel producing a free-stream velocity of 20 m/s (Re = 260,000). A time-resolved particle image velocimetry (TRPIV, 3 kHz) system is used to observe and measure the vortex dynamics in the wake of the baseline flow, the forced flow turbulent characteristics and the dynamic process of the reattachment resulting from a non-thermal plasma actuation operated in continuous (quasi-steady) mode. Post-processing tools such as spatio-temporal correlations or vortex identification are developed to analyze the dynamic of the dominant flow structures. It is expected that the detailed study of the vortex dynamic for stalled case leads to a better understanding of the mechanisms required to improve the effects of the control by single DBD actuator or other control system. The controlled flow will also be documented in terms of time-averaged velocity fields, instantaneous velocity, and vorticity or energy distribution. The final part of this paper deals with the analysis of the vortex dynamic during the forced flow reattachment and typical time-responses of the flow are briefly introduced.

2 Experimental Setup

2.1 Wind test tunnel

The measurements are carried out at the University of Poitiers in an Eiffel-type wind tunnel (open circuit) having a transparent (glass) working section (400 mm high, 300 mm wide and 2,300 mm long). The convergent (contraction ratio of 19:1, 780 mm long) is preceded by a filter, a honeycomb (30-mm wide and 60-mm long cells) and a fine grid (5 mm) located 420 mm upstream of the test chamber entrance in order to provide a uniform flow. A Pitot tube is used to control the free stream velocity at the entrance of the test section. The airfoil is placed in the spanwise direction of the test chamber at an angle of attack of 16°, corresponding to the post-stall regime (Fig. 1). The free stream velocity is set to 20 m/s, resulting in a Reynolds numbers based on the chord length of approximately 2.6×10^5. The airfoil model is placed on a force measurement balance which supports the airfoil profile and allows to fix the angle of attack (here, the force balance is not used). The referential system used in the present paper is shown in Fig. 1.

2.2 Airfoil model

The NACA 0015 model has a chord length of 200 mm and a spanwise length of 296 mm. The model is realized in two separated parts. The first, made of polyurethane, is the scaffold of the model (see Fig. 2). The second is a removable part (insert made of PMMA) which constitutes 80% of the suction side and 20% of the lower camber including the leading edge of the airfoil. This removable part is

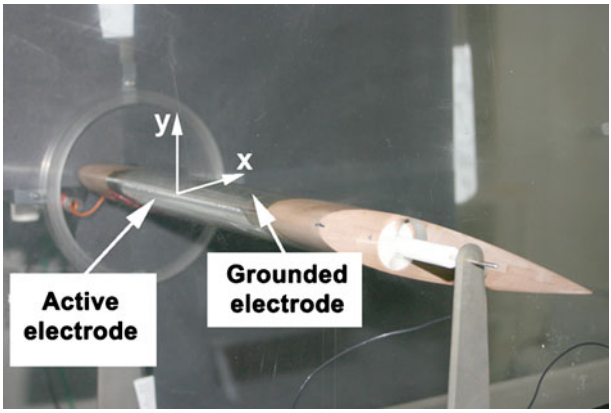

Fig. 1 Airfoil model placed in the test section

3 mm thick and it is used as a dielectric material between the electrodes defining the plasma actuator.

The chord length of the model is chosen to restrict the frequency content of the flow at a reasonable range by using the scale effect. This was motivated by the specifications of our acquisition system. By using a large chord, the temporal and spatial resolution of the measurements is enhanced because flow structures are larger and the frequency content remains low (typically on the order of O(1) kHz). However, a significant drawback is that the span to chord ratio is low and may contribute to three-dimensional effects due to the boundary layer developing on the side walls of the wind tunnel. Based on previously reported PIV measurements for this configuration [17], the variation in the mass flow rate between upstream and downstream locations in the mid plane is approximately 1.8% at 20 m/s. This suggests that three-dimensional effects are limited to the lateral sides and thus do not significantly affect the mid span region. However, a recent experiment has suggested that the separation process is affected by three-dimensional effects that does not change the global dynamic of the separation, but produce significant modification of the time-scale involved in the separation process [18]. Opposingly, the reattachment process remains perfectly reproducible suggesting that 3D effects have less impact on this case that is precisely the purpose of the present study.

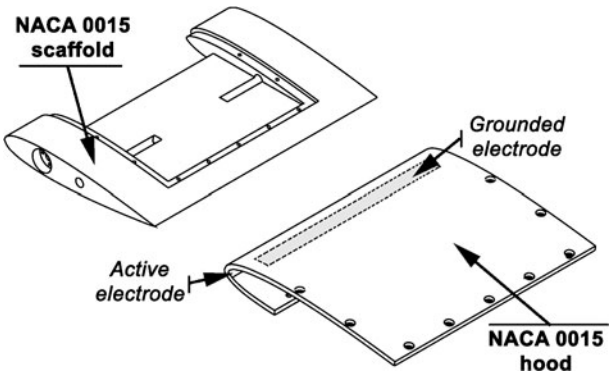

Fig. 2 Sketch of the NACA 0015 profile equipped with a single DBD actuator located at the leading edge

2.3 Plasma actuator design

As shown in Fig. 3, the single DBD consists in two thin aluminium foils (80 μm thick) stuck above and under the 3 mm thick removable insert, acting as a dielectric. The electrode flush mounted upside the dielectric material (active electrode) is connected to the high-voltage supply whereas the second electrode located under the PMMA is grounded. The actuator covers 54% of the span of the airfoil and the edge of the active electrode is located at the leading edge (0% of the chord length), upstream the expected separation point (Fig. 3). The active electrode is 20 mm wide while the grounded electrode is 15 mm wide. There is a small gap of 5 mm between the active electrode and the facing grounded electrode. This asymmetric configuration is chosen according to an optimization study that defined this set-up as the most effective in terms of production of electric wind [14]. The electric wind produced by the electrode arrangement results in a co-flow mode actuation.

The actuation is performed on only 54% of the spanwise. For such a configuration, the finite extent of the actuator may promote three-dimensional flow structures at the tips of the air-exposed electrode. However, it is assumed that the flow remains bi-dimensional in the mid plane of the model.

2.4 Excitation signal

A power amplifier (Trek 30 kV/40 mA, New York, USA) is controlled by a function generator (TTi, TG1010A, Cambridgeshire, England). Continuous actuation is performed by applying a sinusoidal signal to the active electrode (36 kV_{p-p} at 1.5 kHz). In such conditions, an electric wind parallel to the wall of about 4 m/s is expected.

2.5 High-speed PIV system and frame analysis parameters

A time-resolved PIV system (TR-PIV) provided by Lavision company is used in the present study. This PIV setup is composed of a dual-head high-speed laser system (Pegasus, New wave research) which produces 10 mJ at 527 nm when operating at 2,000 Hz. The laser is coupled to a 10 bits high-speed camera (Photron, APX-RS). This camera can be operated at 3,000 full frames per second at mega pixel resolution (1,024 × 1,024) and a reduced resolution can be used, allowing an acquisition frequency up to 10 kHz. In the present study, the acquisition rate is set to 3 kHz. This optimized frequency was defined by preliminary tests for an effective caption of the flow structures dominating the wake region. A synchronizer is used to trigger the TR-PIV with the electrical signal supplied to the actuator. A lens system placed at the laser beam exit forms a thin laser sheet (less than 1 mm). The light system is placed above the airfoil. The laser sheet is perpendicular to the suction side and it

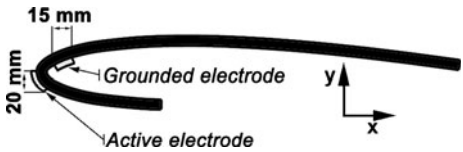

Fig. 3 Electrode configuration of the single DBD

intersects the NACA profile at mid-span position. The CCD camera axis forms a 90° angle with the laser sheet, and the field of view covers the whole chord length of the airfoil (spatial resolution of 1,024 × 528 pixels). The recording procedure consists in double-frame acquisition and the time between two successive images is set to 50 μs.

Fine oil droplets, resulting from the atomization of a pharmaceutical oil (Ondina 15, Shell) by a fog generator (Deltalab, EI511), are used as particle trackers. According to the datasheet of the fog generator, the seeding particles have a diameter ranging from 0.5 up to 2 μm. The frames are analyzed with Davis software (Lavision v7, Goettingen, Germany) and the velocity components are computed using a cross-correlation algorithm with adaptive multipass, interrogation windows of 64 × 64 to 32 × 32 pixels and an overlap set to 50%. The adjustment of the TR-PIV system produces a spatial resolution of 3.68 × 3.68 mm^2 for the vector fields (i.e. image resolution of 0.225 mm per pixel). The images are post-processed with a local median and noise ratio filters in order to detect spurious vectors [19]. The filter computes a local median vector from the eight neighbouring vectors and compares the middle vector with the calculated median. The middle vector is removed and replaced if it differs by more than 1.3 times the root mean square of the median. The confidence in the obtained results is rather high even if a detailed analysis of the PIV fields demonstrates that some image sequences lead to an increase of the number of rejected vector mostly due to inhomogeneous tracers in the flow. However, the mean percentage of rejected vectors remains lower than 3.5% over a whole acquisition sequence (Fig. 4).

Each sequence includes three actuation periods in order to characterize the transition states between the baseline and forced flows. Sequences of 5,980 couples of images are recorded at each acquisition (i.e. acquisition time of about 2 s). This acquisition time is rather short but is statistically sufficient to obtain converged time-averaged values. The Fig. 5 shows typical statistical convergence curves for a single acquisition sequence. The time-averaged velocities are totally converged above the airfoil (see Fig. 5, point 1), in the vortex street (Fig. 5, point 2) and at the trailing edge (Fig. 5, point 4). However, a lower convergence rate appears in the region presenting low local velocity (Fig. 5, point 3). This decrease in convergence rate could be related to a lack of particle tracers in the wake region, few millimetre downstream the flow separation.

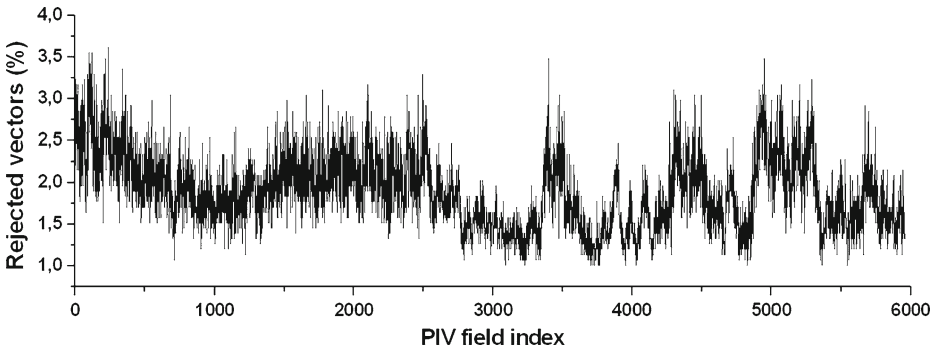

Fig. 4 Percentage of spurious vectors rejected by the local median and noise ratio filters

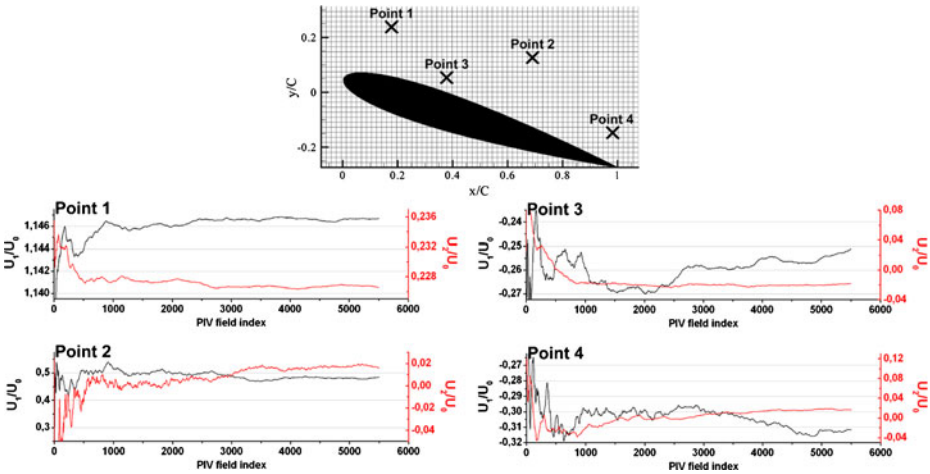

Fig. 5 Typical statistical convergence of the time-averaged velocities

2.6 Data processing

This section is dedicated to the description of the analysis tools developed in order to characterize the flow. Details of the computation of the time-averaged quantities, the vortex identification, the computed correlation or the determination of the integral length scales are successively described in the above sections.

2.6.1 Time-averaged quantities

Classical temporal mean quantities, such as the time-averaged velocity norm or the root mean square values, are calculated. Considering the velocity U_i^t (i = 1,2 for the velocity components in the x and y direction, respectively), the time-averaged velocity norm in non-dimensional form is defined by:

$$\overline{U}(x, y) = \frac{1}{N} \frac{\left[\left(\sum_{t=0}^{N} U_1^t(x, y) \right)^2 + \left(\sum_{t=0}^{N} U_2^t(x, y) \right)^2 \right]^{1/2}}{U_0} \tag{1}$$

where N is the number of PIV fields taking into account for the time-averaged sequence and U_0 refers to the main flow velocity ($U_0 = 20$ m/s). The fluctuating velocity components $u_i^{'t}$ can be deduced by subtracting the time-averaged velocity:

$$u_i^{'t}(x, y) = \frac{U_i^t(x, y) - \frac{1}{N} \sum_{t=0}^{N} U_i^t(x, y)}{U_0} \tag{2}$$

then, the root mean square values $\overline{u_i^{'}}$ which represent the fluctuating velocity are defined by:

$$\overline{u_i^{'}}(x, y) = \left[\frac{1}{N} \sum_{t=0}^{N} \left(u_i^{'t}(x, y) \right)^2 \right]^{1/2} \tag{3}$$

while the root mean square norm is derived from Eq. 3:

$$\overline{u'}(x, y) = \frac{\left[\left(\overline{u_1'}(x, y)\right)^2 + \left(\overline{u_2'}(x, y)\right)^2\right]^{1/2}}{U_0} \tag{4}$$

The turbulent kinetic energy (k) is also derived from the instantaneous PIV results. This turbulent quantity is a relevant parameter to describe a highly dynamic flow as it measures the kinetic energy associated with eddy structures. The instantaneous values of the turbulent kinetic energy can vary substantially, so it is useful to compute a mean value which is more representative of the overall flow. Furthermore, eddy structures are usually highly three dimensional while here, only two velocity components are measured. We assumed that the contribution of the third velocity component is equal to one third of the secondary velocity component. Such an assumption induces that k can be approached by the following expression in 2D flows:

$$k(x, y) = \frac{\frac{1}{2}\left(\overline{u_1'(x, y)^2} + \frac{4}{3}\overline{u_2'(x, y)^2}\right)}{U_0^2} \tag{5}$$

2.6.2 Vortex identification

The flow separation occurring over an airfoil promotes the shedding of coherent structures along the shear layer axis. Different quantities can define and localize such flow structures as reviewed in Bonnet et al. [20]. Two flow quantities are extracted from the PIV fields for eddy localization. The first is the classical local vorticity value ω_z, directly derived from the PIV fields and resulting in a quantity that depends on the accuracy of the PIV results:

$$\omega_z^t(x, y) = \frac{1}{2}\left[\frac{\partial U_2^t(x, y)}{\partial x} - \frac{\partial U_1^t(x, y)}{\partial y}\right] \tag{6}$$

A second quantity, initially described by Michard et al. [21], is retained to characterize the location of the flow structures. This criterion (Γ_1) is only based on the flow topology and thus remains non dependent on the PIV accuracy contrary to the vorticity value. The development of an eddy localization algorithm based on this criterion allows to automatically locate the vortex centres in the instantaneous PIV fields. The treatment over a vector field sequence defines the preferential places of the coherent structures during the experiment history. For the present investigation, the dimensionless scalar function Γ_1 is computed at each P point of the interrogation windows S using:

$$\Gamma_1^t(x_P, y_P) = \frac{1}{N}\sum_S \frac{\left(\overrightarrow{PM} \wedge \left(U_1^t(x_M, y_M)\cdot\overrightarrow{e_i} + U_2^t(x_M, y_M)\cdot\overrightarrow{e_j}\right)\right)\cdot\overrightarrow{z}}{\|\overrightarrow{PM}\|\cdot\left\|U_1^t(x_M, y_M)\cdot\overrightarrow{e_i} + U_2^t(x_M, y_M)\cdot\overrightarrow{e_j}\right\|} \tag{7}$$

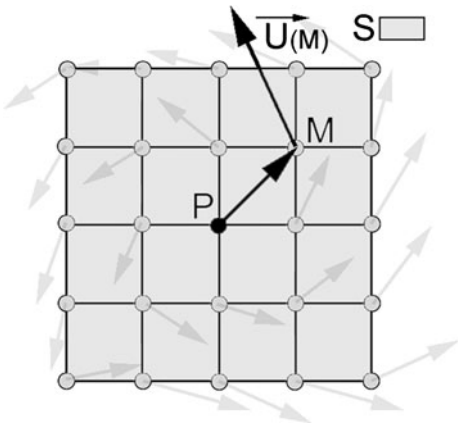

Fig. 6 Integration domain S

where $\vec{z}$ is the unit vector normal to the acquisition plane and N is the number of data points M inside S, area set to a 5 × 5 square domain here (i.e. approximately 14.72 × 14.72 mm^2, see Fig. 6).

A threshold value of Γ_1 (set to 0.8) discriminates the vortex structures from the background flow ($|\Gamma_1|$ is bounded by 1, see Fig. 7a–c). The 5 × 5 square domain acts as a filter for small scale turbulence. Indeed, according to the spatial resolution of the PIV fields (i.e. 3.68 × 3.68 mm), the minimal diameter of the identified vortex structure is about 7.4 mm. Negative values of the Γ_1 criterion correspond to counter clockwise vortices while positive values are associated with clockwise vortices. The vortex centre is identified by the detection of the maximum value of Γ_1 in each of the vortex structure (Fig. 7d). The identification of the vortex structures is based on the analysis of the snapshot fields over sequences characterizing the flow state. This method completes the analysis obtained by using the vorticity fields. Successive locations of the large scale structures can be autonomously obtain over long acquisition sequences.

2.6.3 Correlation functions

In order to take advantage of the PIV fields resolved in space and time, single and multi-point spatio-temporal correlation functions are computed. The single-point temporal correlation function is dedicated to the characterization of the shedding vortex frequency. For instance, a repetitive flow patterns occurring during the sequence acquisition could be identified by the computation of a spatial average of the single-point temporal correlation functions. The normalized single-point temporal correlation function ($R_{ii}(x, y, \tau)$) can be defined at each point of the PIV grid by:

$$R_{ii}(x, y, \tau) = \frac{\sum_t u_i'^t(x, y)\, u_i'^{t+\tau}(x, y)}{\sqrt{\sum_t \left(u_i'^t(x, y)\right)^2} . \sqrt{\sum_t \left(u_i'^t(x, y)\right)^2}} \tag{8}$$

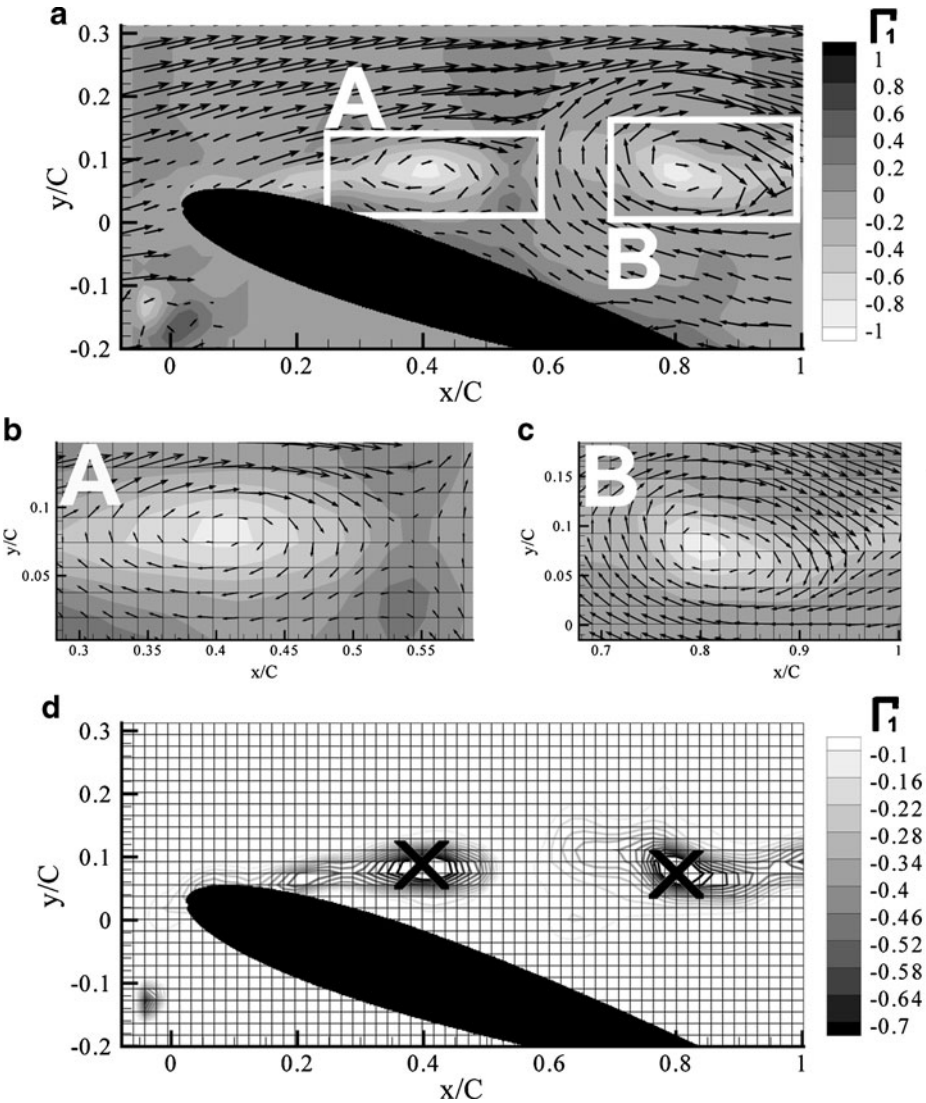

Fig. 7 Illustration of the Γ_1 criterion for baseline flow conditions (**a**). Coherent structures identified by the criterion (**b**) and (**c**). Vortex centre identification for one instantaneous snapshot PIV field (**d**), the *crosses* correspond to the large-scale structure centres while isovalues of the Γ_1 criterion is plotted in background

where τ is the lag time between each correlated vector field couple. An overall estimation of the temporal correlation function is given by:

$$R_{ii}(\tau) = \frac{\sum_{k=1}^{nk}\sum_{j=1}^{nj} R_{ii}\left(x_k, y_j, \tau\right)}{\sum_{k=1}^{nk}\sum_{j=1}^{nj} R_{ii}\left(x_k, y_j, 0\right)} \tag{9}$$

where nk and nj refer to the maximum indices of the PIV grid in the x and y direction, respectively (here, nk = 64 and nj = 33).

According to the accuracy in time and space of the TR-PIV results, second-order velocity spatio-temporal correlation ($R_{ii}(rx, ry, \tau)$) computed at A point (x_a,y_a) can also be defined using the following formula:

$$R_{ii}(rx, ry, \tau) = \frac{\sum\limits_{rx,ry,t} u_i^{'t}(x_a, y_a)\, u_i^{'t+\tau}(x_a + rx, y_a + ry)}{\sqrt{\sum\limits_{t} \left(u_i^{'t}(x_a, y_a)\right)^2} \cdot \sqrt{\sum\limits_{rx,ry,t} \left(u_i^{'t} + \tau\,(x_a + rx, y_a + ry)\right)^2}} \tag{10}$$

Such spatio-temporal correlation is an effective quantity highlighting the time history of a chosen vortex structure. Moreover, the analysis of this correlation function allows to accurately measure the convective velocity of the coherent structure embedded in the shear layer region.

2.6.4 Integral length scale

The integral length scale is an important feature of the flow structures. This quantity measures the mean scale size of the energy containing vortical structures. There are standard turbulence length scales for each of the eddy scale size in a turbulent flow (integral length scale for the coherent structures, Taylor micro-scale for the inertial sub-range and Kolmogorov micro-scale for the dissipation range). It is expected that integral length scales larger than 3.68 mm (according to the spatial resolution of the TR-PIV setup) are associated with the largest eddies of the airflow. Subsequently, a methodology dedicated to the measurement of such a quantity is used. This method is derived from the classical integral length scale estimation based on two-point measurements [22]. An evaluation of the longitudinal (i.e. in the x direction) two-point spatio-temporal correlation ($R_{ii}(y, \eta, \tau)$) is first estimated by using the following formula:

$$R_{ii}(y, \eta, \tau) = \frac{\sum\limits_{\eta,t} u_i^{'t}(x, y)\, u_i^{'t+\tau}(x + \eta, y)}{\sqrt{\sum\limits_{t} \left(u_i^{'t}(x, y)\right)^2} \cdot \sqrt{\sum\limits_{t} \left(u_i^{'t+\tau}(x + \eta, y)\right)^2}} \tag{11}$$

This correlation function is estimated by an iterative process over a PIV field with η being the longitudinal distance between the two correlated points. Typical examples of the spatio-temporal correlation functions are shown in Fig. 8a for eight η values. The axial turbulence integral length scale L can be defined as:

$$L = \int_0^{\infty} R_{ii}(y, \eta, 0)\, d\eta \tag{12}$$

The Fig. 8b illustrates the evolution of the spatio-temporal correlation function versus the separation distance η for a lag time sets to zero. A numerical integration based on the trapezoid method can automatically calculate the integral length scale L.

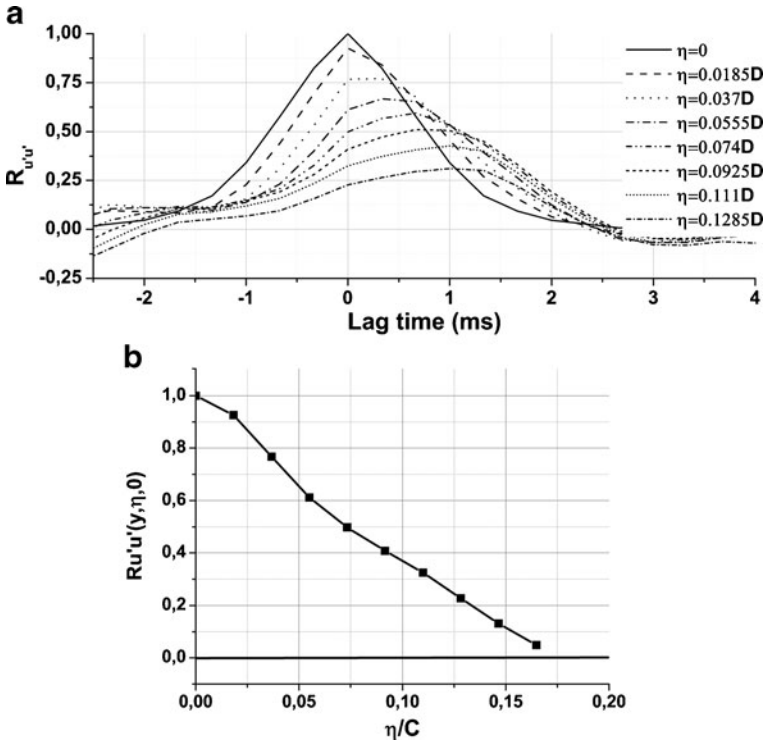

Fig. 8 Typical spatio-temporal correlation function of the baseline flow at different separation distance (**a**) and typical evolution of the correlation coefficient at $\tau = 0$ versus the separation distance (**b**)

3 Results

The analysis of the results is separated in different parts. The first one focus on a detailed investigation of the baseline flow to fully describe the main characteristics of the vortex street occurring from the leading edge. A second part is assigned to the description of the airflow induced by the DBD actuator without surrounding airflow. Effects of the DBD actuation on the naturally separated flow are also described. The last part of the paper deals with a time-resolved analysis of the flow reattachment dynamic.

3.1 Baseline flow

3.1.1 Time-averaged velocity fields

The time-averaged velocity field for baseline flow confirms that the observed flow is in post-stall regime (incidence of 16°) with a large region naturally separated from the suction side, resulting in a strong adverse pressure (Fig. 9). The result shown in Fig. 9a demonstrates that the boundary layer separation occurs approximately at x/C = 0.1 and y/C = 0.05 that corresponds to 5% of the chord length. The location of the separation point agrees pretty well with the literature data [23–25]. As it is

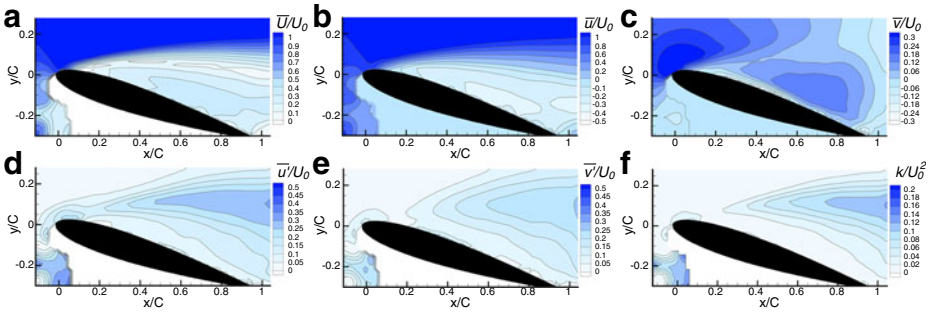

Fig. 9 Time-averaged PIV fields, (**a**) velocity norm, (**b**) primary velocity component, (**c**) secondary velocity component, (**d**) primary component of the fluctuating velocity, (**e**) secondary component of the fluctuating velocity and (**f**) turbulent kinetic energy for baseline flow with external airflow at $U_0 = 20$ m/s

usually observed at this angle of attack, the flow separation results in formation of a single separation bubble delimited by a free shear layer [26]. This recirculation has here a cross-stream extension of 0.44C. The maximum velocity norm in the recirculating region is approximately 0.3–0.4U_0, and the flow above the separated region undergoes an increase of 16% compared to the free stream velocity. The fluctuating region above the suction side of the airfoil illustrates the presence of a free shear layer (Fig. 9d and e). High levels of fluctuating velocity are observed starting from x/C = 0.4. These are directly related to the coherent flow structures in the vortex street. This vortex activity is confirmed by the turbulent kinetic energy distribution (Fig. 9f). In particular, the peak level observed above the trailing edge of the airfoil indicates the presence of highly energetic structures at this location.

3.1.2 Spatio-temporal characterization of the vortex street

In this section, a particular attention is paid to the analysis of the vortex street issuing from the boundary layer separation. The analysis of the vortex shedding is performed by the identification of the spatial position of the coherent structures, by the computation of the vorticity and by the estimation of the spatio-temporal correlation functions. Such post-processing tools should be adequate for a detailed analysis of the vortex dynamics.

As demonstrated by other authors [21, 27], the Γ_1-criterion is a useful processing tool to identify the coherent structures embedded in a turbulent flow and locate theirs centres. The application of this criterion over a whole TR-PIV acquisition sequence allows to describe the successive preferential positions of the vortex centres. As it is usually reported, the separation over a NACA results in the formation of small scale vortices that grow and energize along the free shear layer axis [28–30]. An illustration of a vortex street containing three successive large scale structures is plotted in Fig. 10a. The detection of the coherent structure centres over the acquisition sequence (approximately 5,000 snapshots) reveals that the flow remains fully detached along the full chord length (Fig. 10b). Furthermore, the eddy structures have no preferential location, but they locate between the upper and lower free shear layer as defined by the fluctuating region in Fig. 9d. Another important result concerns the sense of rotation of these vortical structures which remains always in a clockwise sense. The momentum transfers (from the high velocity region toward

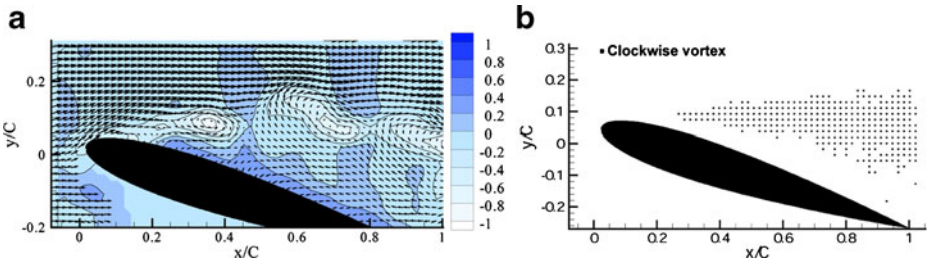

Fig. 10 Γ_1-criterion for an arbitrary instantaneous PIV field (**a**) and spatial location of the vortex centres over 5,900 instantaneous PIV field (**b**)

the lower one) are not strong enough to promote intermittent reattachments for the considered acquisition sequence.

The spatio-temporal evolution of the vortex structures can be characterized by analysis of vorticity, vector fields and Γ_1-criterion values (Fig. 11). The core of each coherent structure at eight different times is visible in Fig. 11. The vortex shedding is clearly visible in the velocity field. The evolution of the vortices from the leading to the trailing edge can be identified. This suggests a bi-dimensional flow in the investigated field of view despite a low aspect ratio. As expected for a bi-dimensional flow, the vortex shedding is characterized by flow structures rolling up along the free shear layer axis with a clockwise sense of rotation. A high vorticity region initiates downstream the separation point, at approximately 5% of the chord length. This suggests that a distance of approximately 8 mm is necessary for the Kelvin-Helmholtz to develop in coherent vortical structures. Discrete large scale flow structures start to shed at roughly x/C $\sim$ 0.45 but their formation initiates further upstream at x/C $\sim$ 0.25. Theses structures are convected at initial speed of about 8–10 m/s, but it is expected that this convective velocity decreases further downstream. The individual coherent structures grow and strength when they are convected along the shear layer axis. The roll-up of the shear layer can induce a coalescence process (at x/C = 0.8–0.9 for times between 0 and 3.33 ms, or at x/C = 0.4 for times between 6.66 and 11.66 ms, for instance). Downstream x/C = 0.9, vorticity regions dislocate due to the freestream turbulence as it was numerically observed [25].

The spatio-temporal correlation function R_{22} is computed in free shear layer location in regard to the mid-chord position (x/C = 0.6 and y/C = 0.15) (Fig. 12). According to Fig. 11 (at time 10 ms), this location is at the centre of the free shear layer where probability to see a large-scale flow structure is high. The function is computed on the secondary velocity component, subsequently highlighting the dominant spatio-temporal evolution of the coherent flow structures passing by the point x/C = 0.6 and y/C = 0.15. The analysis of this spatio-temporal correlation function complete the time-evolution of the flow structures identified by the vorticity fields. As previously observed from the vorticity representation, flow structure with positive value is initially formed downstream the boundary layer separation. This

Fig. 11 Typical temporal evolution of the large scale structures identified by the Γ_1-criterion value ▶ (*left column*) and by the local vorticity (*right column*)

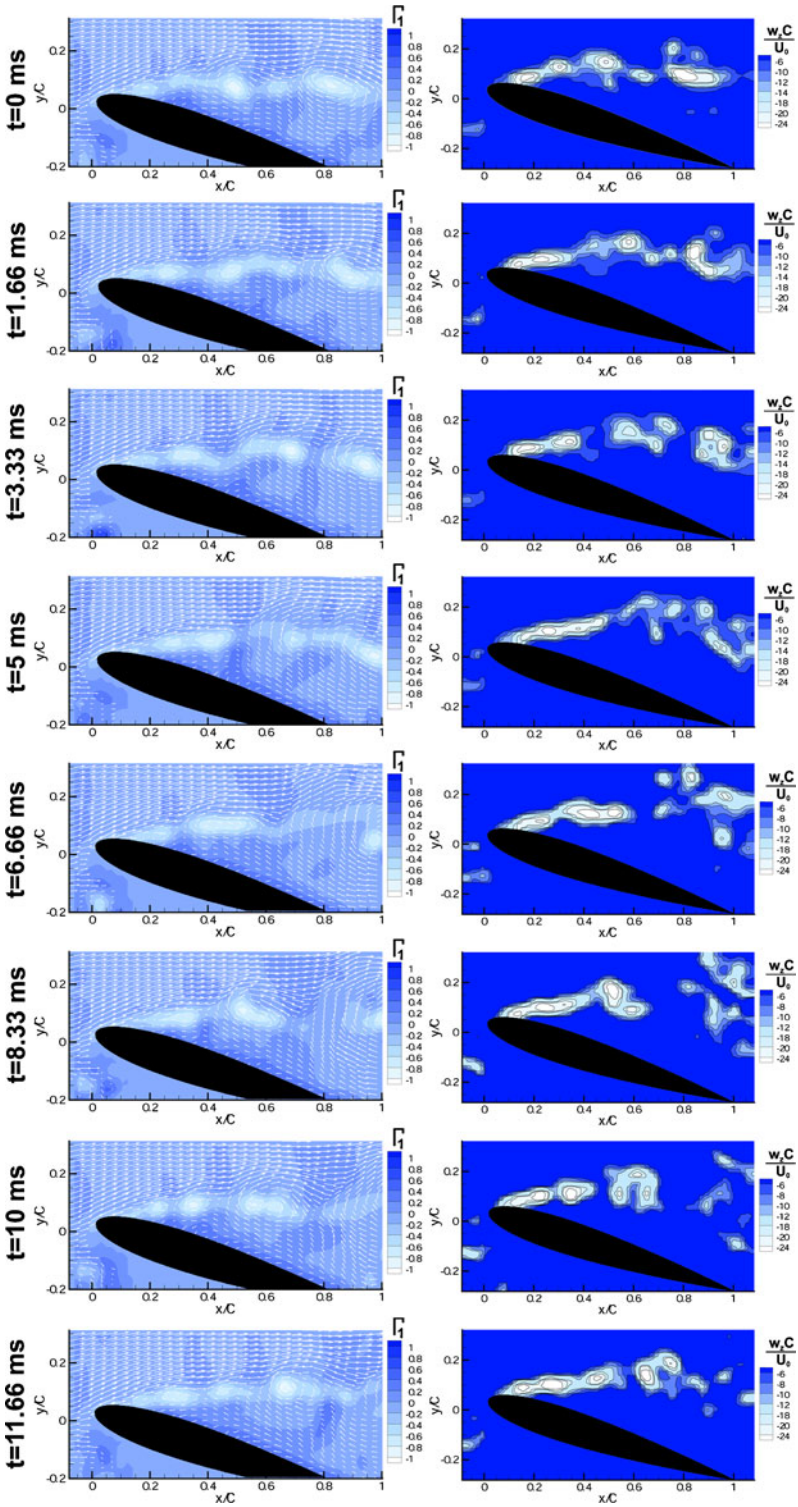
t=0 ms
t=1.66 ms
t=3.33 ms
t=5 ms
t=6.66 ms
t=8.33 ms
t=10 ms
t=11.66 ms
x/C
y/C
Γ1
wzC/U0

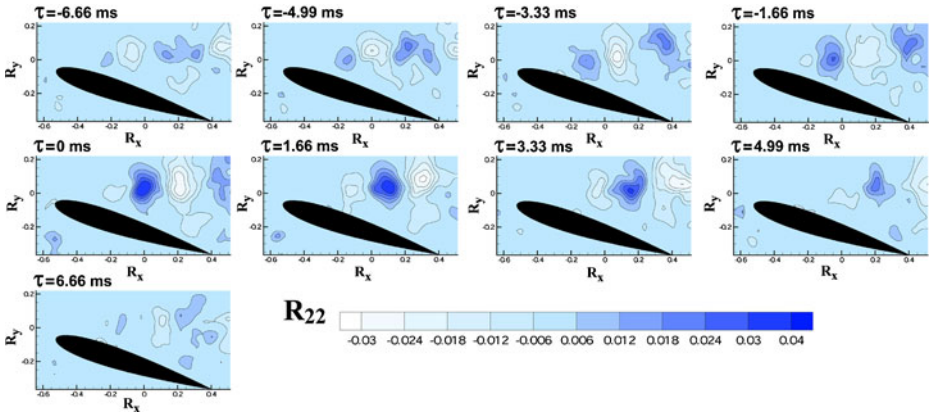

Fig. 12 Spatio-temporal correlation function R_{22} (calculated on secondary velocity component)

structure grows and becomes stronger along the shear layer axis. The correlation function clearly reveals that the flow structure losses its coherency at $\tau > 5$ ms. Then, the lifetime for the flow structure can be estimated roughly equal to 12 ms. At a location above the trailing edge, the structure splits in two distinct regions (Fig. 13, regions A_1 and A_2). A portion of the coherent structure is simply convected in the x direction (A_1) while a secondary portion is moved toward the suction side (A_2). After dislocation, the produced two rotating regions should contribute to the mutually interacting vortices in the wake of the airfoil, and promote a highly turbulent wake flow [30].

Considering the frequency acquisition of the TR-PIV system, it is postulated that the natural vortex rollup frequency (f_{st}) is measurable if one exits. For this purpose, the single-point temporal correlation functions are computed at each point of the PIV grid. The estimation of $R_{ii}(\tau)$ over the whole PIV field is performed by a spatial averaging of the correlation functions for each shedding sequence (see Eqs. 8 and 9). In fact, if a flow pattern is repeated over the acquisition sequence, the correlation function distribution should present regular oscillations with a quasi-constant period. As expected, the single-point correlation function (Fig. 14) oscillates with a roughly constant period that corresponds to a frequency of 90 Hz (confirmed by the FFT of the correlation Function). This result indicates that repetitive flow patterns are reproduced at frequencies of 90 Hz that corroborates the lifetime of the coherent

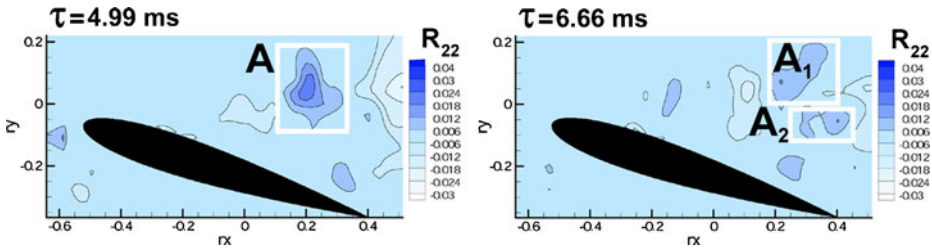

Fig. 13 Preferential spatial location during the vortex dynamic

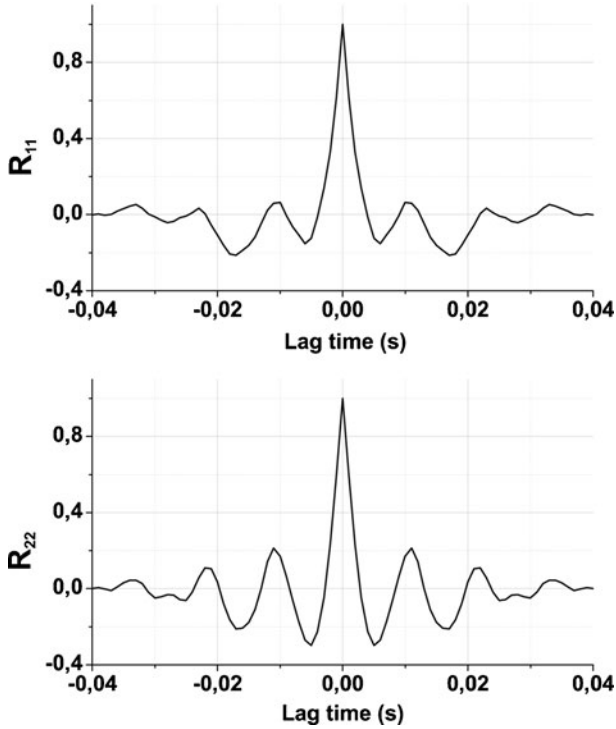

Fig. 14 Temporal cross-correlation functions for naturally separated airflow

flow structure. It is postulated that the trace in the correlation function corresponds to the vortex shedding signature (the governing Kelvin-Helmholtz instability frequency is an order of magnitude higher). In the present study, the reduced frequency $F^+ \left(F^+ = \frac{f_{st}*c}{U_0}\right)$ is equal to 0.9, while the non-dimensional frequency based on the chord length and the angle of attack $\left(f^+ = \frac{f_{st}*c\sin\alpha}{U_0}\right)$ is equal to 0.25. This later frequency is reasonably similar to the reduced frequency observed in the wake of a cylinder [31, 32]. This supports the idea that a same instability process is involved in both aerodynamic configurations. Previous studies have demonstrated that a separated flow is highly sensitive to an excitation performed at a reduced frequency $F^+ = 1$ [26, 33, 34]. Such an unsteady actuation promotes a stable flow reattachment and a significant lift improvement. It was also observed that flow over an airfoil can be reattached and exhibited an optimized lift if the flow is excited by perturbations at $f^+ \sim 0.2$ [35]. As indicated in Mittal et al. [36], excitation of the most amplified instability is one of the scenarios to reach optimal flow control.

A last analysis of the baseline flow concerns the computation of the integral length scale in the x direction (Fig. 15). This scale is an estimation of the growth and decay in size of the most energetic structures developing along the free shear layer region. The methodology used to compute such quantity is defined in Section 2.6.4. The evolution of the turbulent structures along the free shear layer is conventional: the size of the structures growths with the distance from the region where the flow structures initiate (Fig. 15a). The integral length scale is now extracted along an axis roughly matching to the centre of the developing free shear layer (Fig. 15b). It is postulated that this line

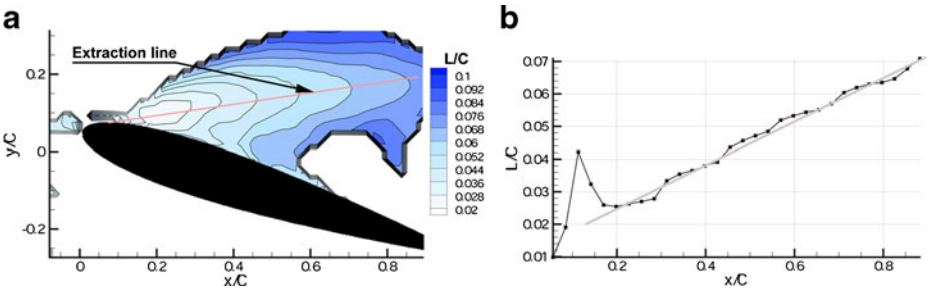

Fig. 15 Integral length scale in the x direction **a** over the whole PIV field and **b** line extraction of the integral length scale along the free shear layer axis. The *grey line* in (**b**) corresponds to a linear fit

corresponds to the location of the vortex street and subsequently relates to position where the coherent turbulence is maximized. According to Fig. 15b, the scale of these structures ranges from 0.02 C up to 0.07 C and a linear dependence between the scale and the position along the free shear layer axis can be found. The integral length scale linearly increases along the shear layer axis according to the relationship $L/C = 0.0668x/C + 0.0118$.

3.2 Airflow induced by the DBD actuator

This brief section is dedicated to the characterization of the airflow produced by the DBD actuator. For this purpose, TR-PIV acquisitions are performed for flow in initially quiescent condition. The spatial resolution of the PIV arrangement (about 4×4 mm^2) is too large to visualize the electric wind in the first millimetres of the boundary layer. However, the global fluid motion generated by the DBD actuator can be accessed. Continuous actuation is here considered that means an actuation turned on at t = 0 ms and maintained during 2 s. The visualization by tracer particles of the plasma-induced electric wind is shown in Fig. 16. This figure reveals that it is produced tangentially to the leading edge curvature. In initially quiescent condition, the actuation produces a large counter-clockwise vortex. A typical duration of approximately 60 ms is required to form a vortical flow structure.

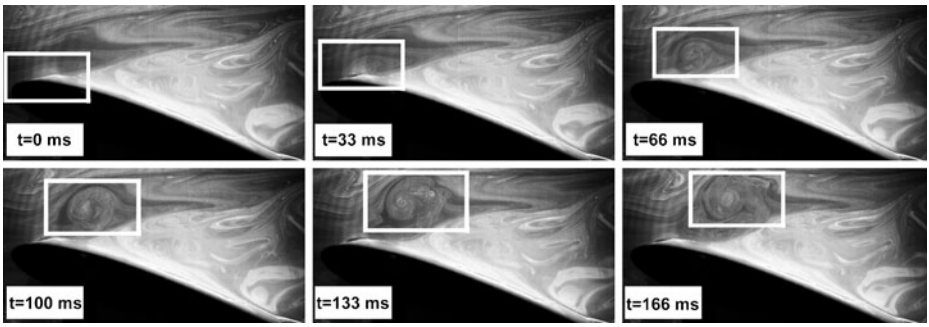

Fig. 16 Visualization by tracer particles of the airflow produced by a DBD actuator operating in continuous mode (initially quasi quiescent flow)

The velocity vector fields resulting from the PIV computation are shown in Fig. 17. As mentioned from the visualizations, the DBD actuator operating in initially quasi quiescent flow produces a large flow structure rotating in counter-clockwise sense. This vortical flow structure, often called *starting vortex*, was widely observed by experiments [37, 38] or by numerical simulation [39]. This flow structure is initiated between 20 and 40 ms after the ignition of the discharge. The response time of a DBD actuator is largely shorter than 30 ms. Indeed, it was previously observed that the electric wind at one millimetre above the electrode can be driven at the electric frequencies applied to the actuator [40]. The AC voltage produces fluctuating velocity at AC frequency (here $f_{AC} = 1$ kHz), but, the formation of the large scale starting vortex requires more time to be fully established. One can observed that a backward flow of about 0.1 ms/ exists on the top part of test section when initial quiescent condition was expected. This backward flow may delay the formation of the starting vortex, but it is postulated that the flow dynamic remains unchanged. According to the applied high-voltage signal, the electrode configuration and the dielectric thickness, the momentum transfer should result in a velocity of 4–5 m/s, in co-flow mode, tangentially to the airfoil profile [11]. This velocity is attained in the vicinity of the boundary layer, a region that cannot be investigated by the present TR-PIV setup. The present measurements show the overall electric wind formation for external flow at quasi resting conditions. However this dynamic may totally differ when an external flow exists. In particular, it is not sure that the large scale flow structure promoted by the discharge interacts with the main airflow due to it very low velocity. Moreover, it is not guarantee that the starting vortex can be formed

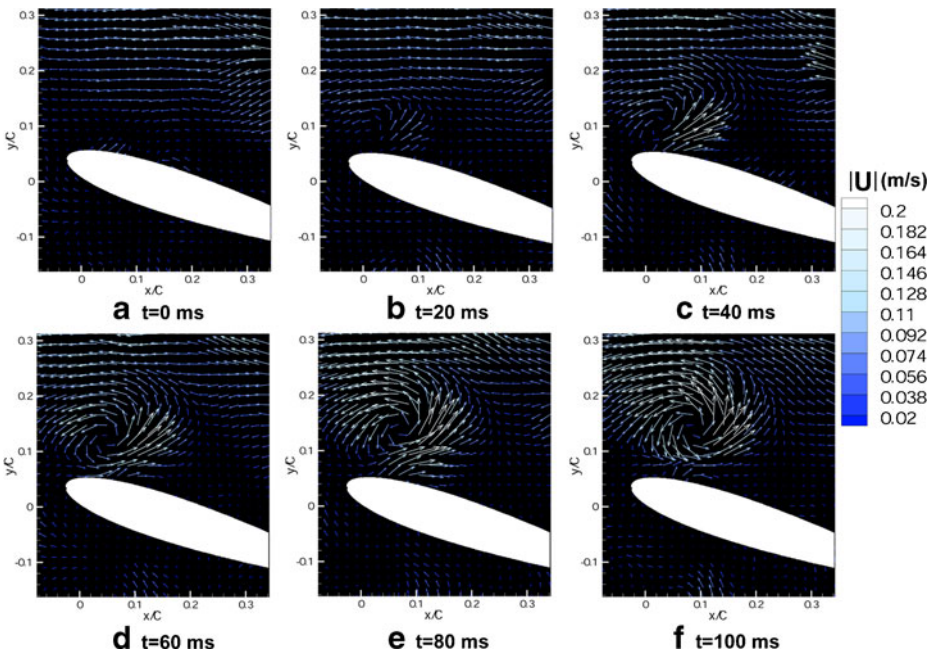

Fig. 17 Velocity vector fields for DBD actuator operating in continuous mode

due to the strong competition between a cross flow and the weak momentum transfer produced by the surface plasma. This point will be discussed later in this paper.

3.3 Flow forced by a DBD plasma actuator operating in continuous mode

In this section, the manipulated airflow resulting from the actuation by a single non-thermal plasma device is described. Results in terms of time-averaged and time-resolved PIV velocity fields are presented.

3.3.1 Time-averaged velocity fields

The time-averaged vector fields confirm the drastic flow changes due to the control strategy. The airflow naturally separates at 0.05 C downstream of the leading edge. Actuation results in a reattachment up to 70% of the chord length (Fig. 18a). This agrees with the background literature that clearly supports a sufficient effectiveness of DBD actuation to increase the lift of NACA profile in post-stall regime at the present Reynolds number [1–8]. The change in flow state also induces modifications of the turbulent velocities in the wake region. In particular, a turbulent intensity reduction is observed in the wake region while the fluctuating velocities are increased at the leading edge (Fig. 18b and c). This latter increase is subsequent to the unsteady nature of the produced electric wind [14, 40]. As revealed in Fig. 18f, the reattached flow exhibits high turbulent kinetic energy at a small distance above the suction surface. This increase in kinetic energy could result from the presence of vortical structures along the suction side.

A transitional effect from a laminar to turbulent state is often suspected to be responsible for airflow reattachment by using non-thermal plasma discharges. Then, one cannot be sure that a similar process would be observed if the initial natural flow was fully turbulent. However, the implication of a transition in the control process is discarded by additional experiment. It has been verified that the natural flow remains fully detached when the laminar-to-turbulent transition is obtained by a tripper placed at the leading edge. The lift experienced by this airfoil in similar experimental conditions was already measured by a force balance in a past study [41]. The evolution of the lift coefficient presents a sudden lift loss when stall occurs. This sharp lift drop is typical of a laminar separated flow. Furthermore, the control

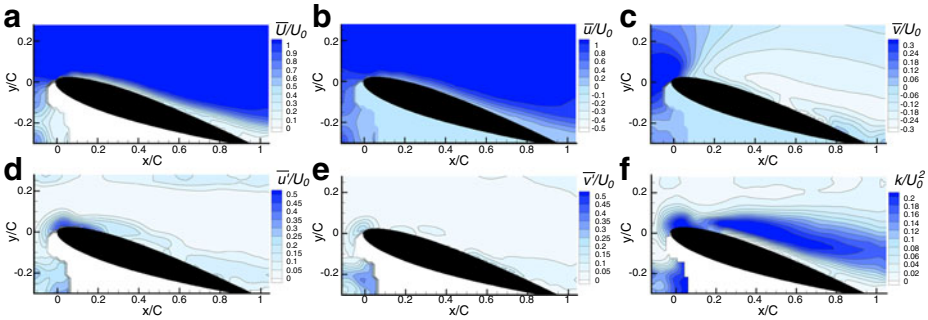

Fig. 18 Time-averaged PIV fields, **a** velocity norm, **b** primary velocity component, **c** secondary velocity component, **d** primary component of the fluctuating velocity, **e** secondary component of the fluctuating velocity and **f** turbulent kinetic energy for airflow reattached by plasma actuation

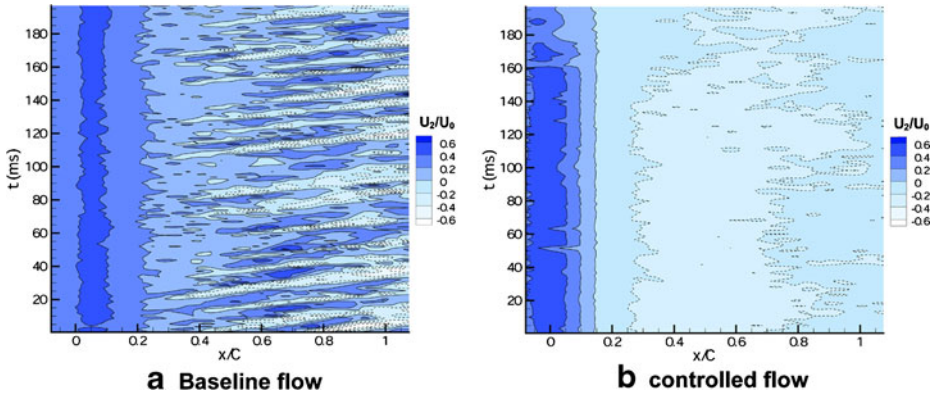

Fig. 19 U_2-component of velocity along y/C = 0.1 as a function of x/C versus time

effectiveness was not affected by the presence of a turbulent boundary layer due to a tripper device. These points support that the mechanism behind the observed control is not related to a laminar-to-turbulent transition.

3.3.2 Unsteady characterization of the controlled flow

In some cases, the forced flow reattachment along the suction side of an airfoil suffers from transitional and unsteady effects such as periodic changes between attached and separated states [42]. In order to prove that no large separation occurs during the actuation period, U_2-component of velocity is extracted along an horizontal line located at y/C = 0.1. The velocity as a function of time and space can then be plotted over the entire acquisition sequence. The Fig. 19 presents the velocity contours as a function of x/C versus time for baseline flow (Fig. 19a) and controlled flow (Fig. 19b). The baseline flow clearly presents a succession of low and high velocity fluid packets,

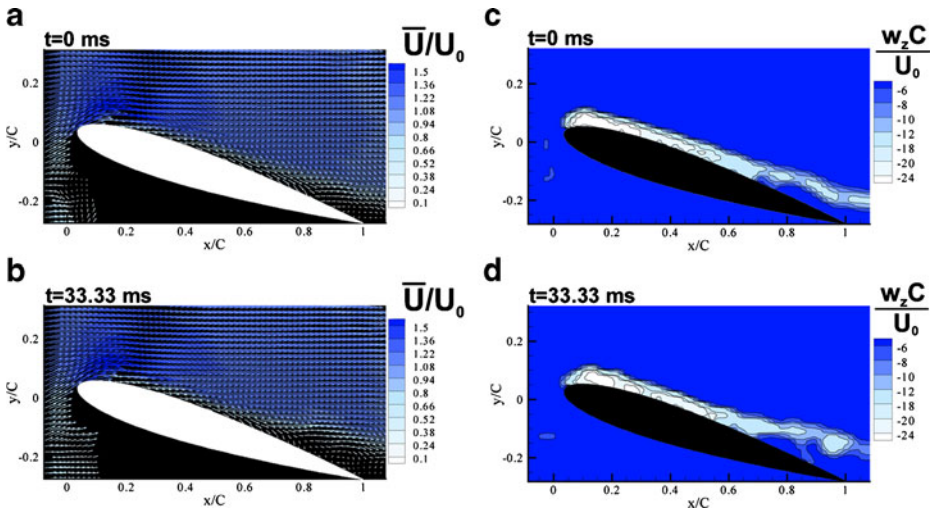

Fig. 20 Typical instantaneous PIV vector fields (**a**, **b**) and associated vorticity (**c**, **d**)

highlighting the vortex street. The temporal evolution of the controlled flow totally differs. The U_2-component of velocity remains low over the entire time record. This indicates that flow remains attached at the leading edge, this without intermittent separated regimes.

The analysis of the instantaneous vectors fields confirms the flow reattachment up to 70% of the chord length. Downstream this position, a moving separation point appears, initiating a partial flow detachment at the end of the airfoil profile (Fig. 20a, b). A region of high vorticity occurs above the suction side up to 95 mm from the airfoil surface (Fig. 20c, d). The boundary layer incurs high vorticity activity up to x/C = 0.7 while, beyond this position, the vorticity is concentrated in a line that is detached from the model. This vorticity region is unstable and detached regions of vorticity finally form and are then convected in the airfoil wake. This result indicates that a new vortex street is formed in the wake, at the end of the reattached region.

The velocity components at x/C = 0.95 and y/C = −0.16 are extracted and plotted as a function of time (Fig. 21a). The alternation of positive and negative values in the U_2-component of velocity confirms a flow structure shedding taking place above the trailing edge. The single-point correlation of this signal reveals a characteristic frequency (f_{wake}) equal to 100 Hz (Fig. 21b). Unfortunately, the field of view is too small to perform a complete description of the far-field wake flow. However, the history of the vortex shedding can be access by computing the spatio-temporal

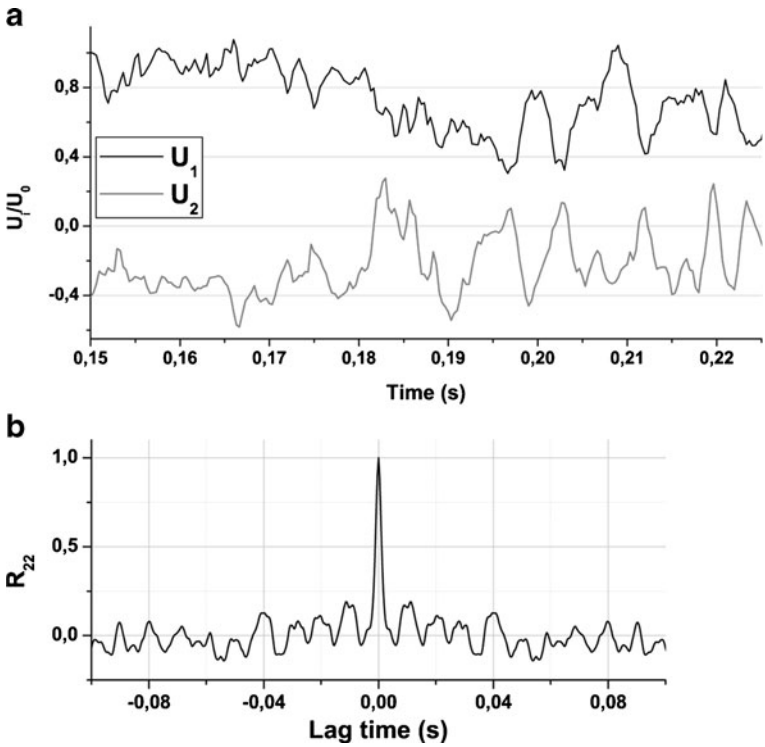

Fig. 21 U_i-component of velocity as a function of time (**a**) and single-point correlation function R_{22} (**b**). Data are collected close to the trailing edge (x/C = 0.95 and y/C = −0.16)

correlation functions at x/C = 0.9 and y/C = −0.2. The Fig. 22 confirms that flow structures are formed at the shifted separation point and not from the leading edge (Fig. 22 at $\tau = -3.33$ ms). This flow structures are finally convected outside the field of view (Fig. 22 at $\tau = 1.66$ and 3.33 ms). A rough estimation of the wake width (δ) based on the time-averaged velocity field indicates a value of approximately 0.12 C. Then, the value of $f_\delta^+ \left(f_\delta^+ = \frac{f_{wake}\delta}{U_0} \right)$ equals 0.12 which approximately corresponds to the typical dimensionless frequency associated with the roll-up of a separated shear layer into discrete vortices in a wake flow ($f_\delta^+ \approx 0.18$, according to Darabi and Wygnanski [43]). The computation of the reduced frequency, f^+, gives a value of 0.27. These reduced frequencies were already observed in unforced wake of various aerodynamic bodies. Subsequently, it seems that the actuation by plasma at the leading edge of the airfoil does not affect the natural frequency of the vortex shedding issuing from the trailing edge.

3.4 Reattachment process by non-thermal plasma actuator

The observation of the flow reattachment forced by a single DBD actuator is not new [1, 2]. However the reattachment process is rarely introduced. Usually only predictive observations are introduced. Here, it is expected that the temporal and spatial resolutions of the acquisition system are suitable to fully describe the processes involved in the forced flow reattachment.

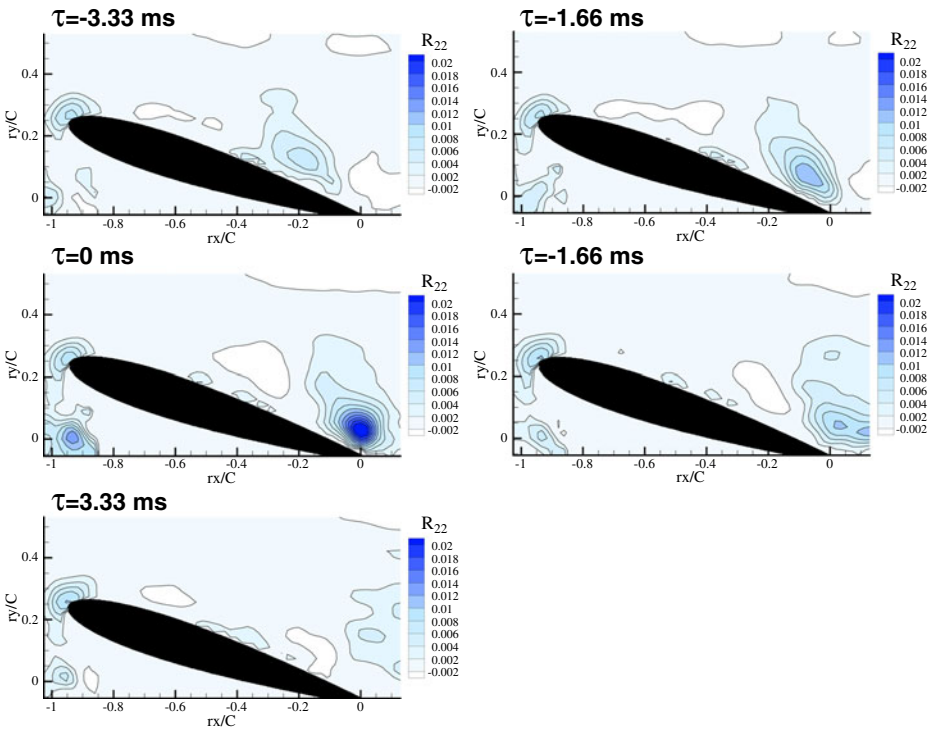

Fig. 22 Spatio-temporal correlation functions R_{22} of the reattached airflow

A simple method to observe the dynamic of the airflow reattachment simply consists in plotting the instantaneous vector fields of the PIV sequence, with here the Γ_1-criterion values in background (Fig. 23). In complement, the instantaneous vorticity fields are provided in Fig. 24.

Surprisingly, there is no counter-clockwise vortex during the reattachment process contrary to the measurements performed with DBD actuators operating in quiescent air (Fig. 17). In fact, the velocity and vorticity of the gas flow produced by the actuator is one order of magnitude lower than the external velocity speed. The electric wind produced by the actuator is here too small to produce a large scale counter-clockwise vortex. This was verified over the acquisition sequence that involves three successive continuous actuations producing three successive reattached flows. A fine analysis of the reattachment process reveals a highly reproducible control process. At the initial time step t_0 (time at which the DBD is switched on), the separated

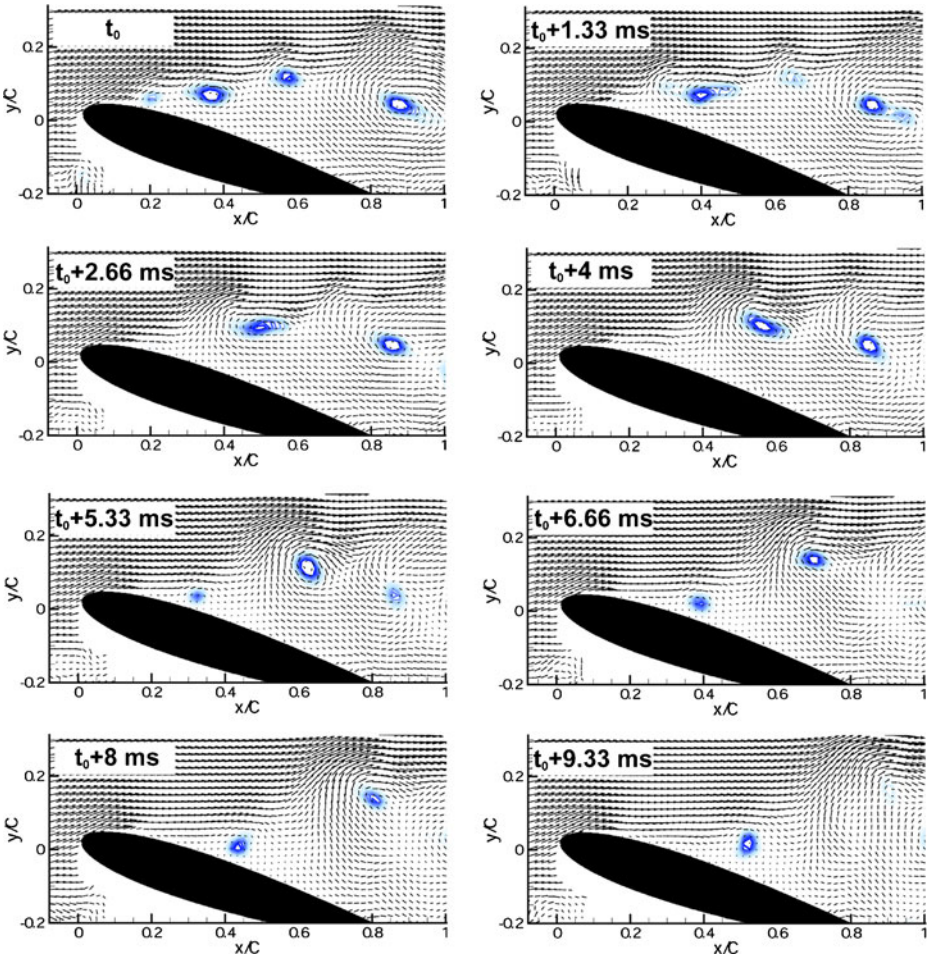

Fig. 23 Vector velocity field during the reattachment process. The background presents the Γ_1-criterion value highlighting the core of each vortex

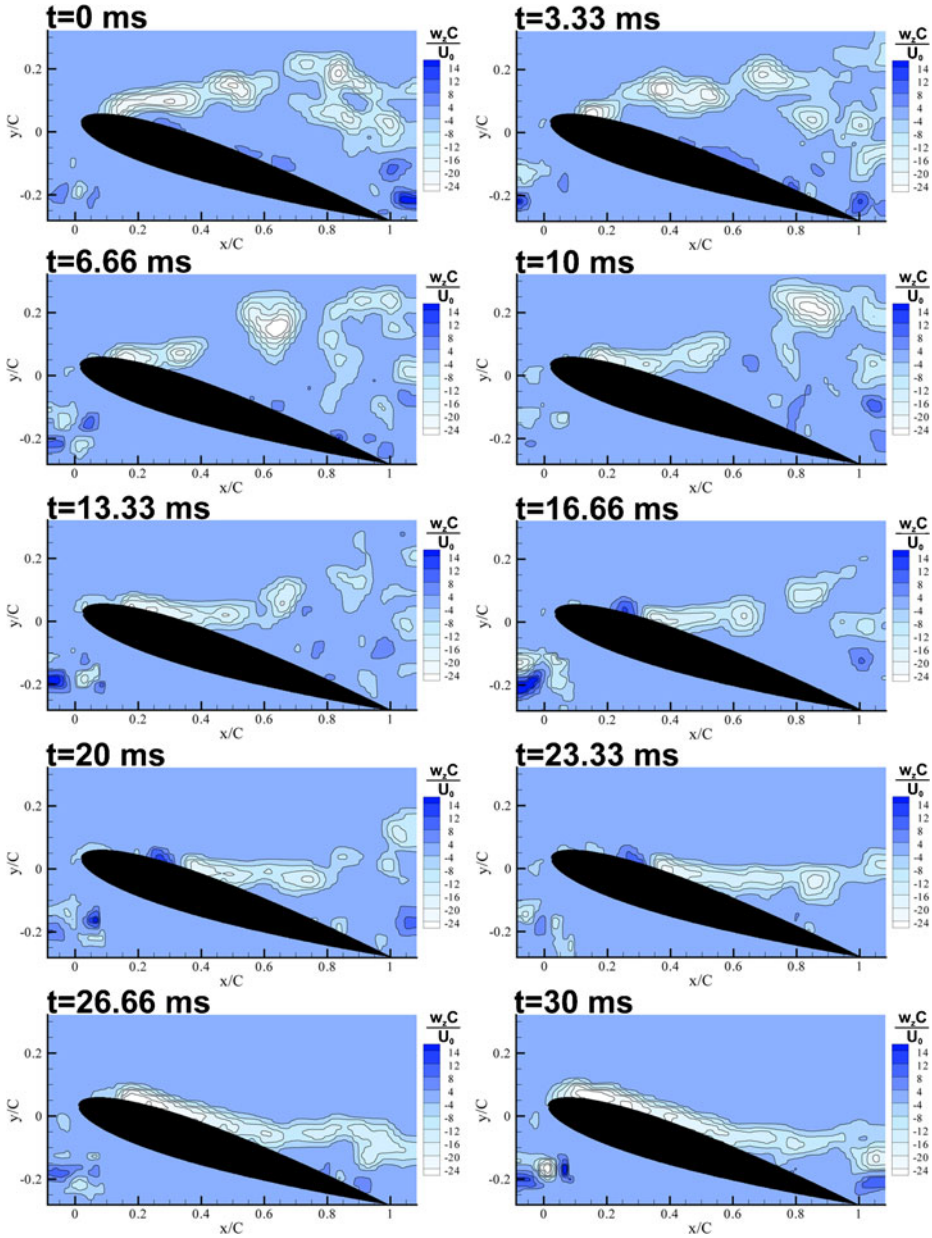

Fig. 24 Instantaneous vorticity field during the reattachment process (forcing is initiated at t = 0 ms)

shear layer presents two vortices along its axis and a large scale structure located above the trailing edge (Figs. 23 and 24). The first effect of the DBD actuation is identified at t = 1.33–3.33 ms. At this time, the airflow produced by the actuator can force a merging of vortices or simply energize a single vortex in the region of interaction between the produced and natural airflows. The size and the strength of this vortex is enhanced by the actuation. The reinforced vortex promotes a

momentum transfer from the outer flow to the boundary layer of the suction side (Fig. 23 at $t_0 + 4$ ms, Fig. 24 at t = 6.66 ms). This change in flow topology should be responsible for a reduction of the adverse pressure gradient. However, this structure initiates a velocity front normal to the suction surface where U_1 velocity component is negligible compared to U_2-component. This vortex rolls up along the shear layer axis, producing a shifting movement of the velocity front along the suction side. This process is the first step of the flow reattachment but is not sufficient to reattach the flow. The high-speed acquisitions indicate that the second vortex issuing from the shear layer is mainly responsible for the reattachment (Fig. 23 at t_0 + 5.33 ms). This second vortex is not convected along the shear layer axis. A combination of the flow change in the wake of the primary large structure and the jet flow resulting from the plasma discharge may be responsible for a new vortex trajectory. The primary vortex conduces to a positive pressure gradient in its wake that locally decelerates the flow and, at one third of the chord length, produces a thicker boundary layer. In the same time, the jet flow formed by the actuator at the leading edge promotes a negative pressure gradient on the suction side and forms a co-flowing shear layer with the main flow. It is postulated that the deviation in the secondary vortex trajectory results from these two aspects. The trajectory of this secondary vortex is moved along the suction side, into the boundary layer region where the pressure gradient is favourable. The sense of rotation of this structure enhances transfer momentum to the boundary layer region by increasing the mixing between the low momentum fluid close to the surface and the outer parts of the boundary layer. This vortex (systematically located at the front of the reattached region) rolls along the suction side of the airfoil at a velocity of 5 m/s and is responsible for the flow reattachment (Fig. 22 at t_0 + 8 ms, Fig. 24 at t = 10 ms). By this process, the flow structure reaches approximately 70% of the chord length, the structure then detaches from the suction side and is convected outside the field of view.

Finally, the momentum transfer responsible for the flow reattachment comes from the outer flow and not from the actuator itself. The DBD actuator acts as a catalyser. The control process is based on a reinforcement of the vortex shedding (Fig. 25a). However, the reinforcement process cannot be fully elucidated by the present study as it requires a statistical analysis with measurements zoomed on the leading edge region. The DBD may amplify the natural instability, resulting in an earlier vortex formation. By this way, the size of the flow structures should be larger and could interact with the boundary layer. Another option is the reinforcement of an already existing flow structure (Fig. 25–2a). In this case, the jet flow produced by the discharge contributes to an increase in negative vorticity by favourably shearing one side of the rotating structure. A last scenario is the merging of two natural vortices or a forced coalescence of successive small-scale flow structures (Fig. 25–2b). The final reattachment results from a strong interaction between the energized vortex convected along the shear layer axis and the small vortex rolling-up along the suction side (Fig. 24–3). One can remark that the DBD actuation seems contribute to only one flow structure contrary to flow control performed by synthetic jets. Indeed, it was experimentally [44] and numerically [45] demonstrated that the lift increase observed for stall control by synthetic jet is due to the creation of two or three vortices convected along the suction side of a NACA 0015 airfoil. Phase-averaged PLIF visualisations have also demonstrated that the coherent structures responsible for the apparent reattachment could coalesce to form a single, more intense vortex synthetic

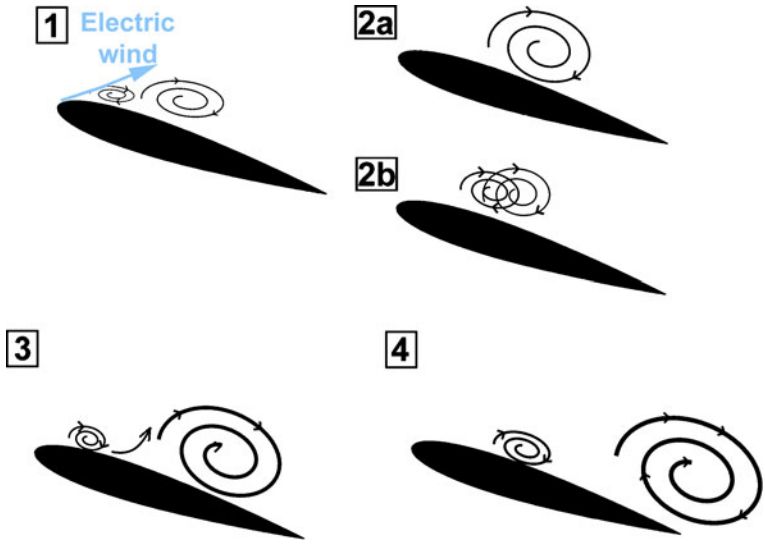

Fig. 25 Sketch of the reattachment process

jets are used [46]. Plasma actuation process slightly differs due to the weak gas flow produced by the discharge. The control device cannot create discrete structures with favourable negative vorticity. An efficient control requires a fine interaction with the already established vortex dynamic.

Nevertheless, the present time-resolved description of the flow control process opens new insights for future experiments. For instance, it demonstrates that the use of several successive plasma actuators placed at the leading edge is not necessarily the most efficient way to improve the control authority. On the contrary, the addition of a second actuator located at mid-chord and producing a flow in the opposite direction compared to the primary airflow would results in a stronger vortex rolling-up along the suction side and might significantly improve the effects of the control by non-thermal plasma. This should been investigated by further experiments.

In a last effort, , velocity data are collected at two locations along the suction side of the airfoil in order to obtain the typical times required to force the flow reattachment (Fig. 26). The first sensor (the closest to the DBD actuator) is the most sensitive to the flow modifications resulting from the actuation. At this location, the first changes in the flow are observed at t $\approx$ 20 ms. These changes are mainly composed of a velocity increase that is representative of a flow reattachment. The typical time necessary to reach a constant behaviour is roughly 35 ms (the over and undershoot in velocity are due to a lack of particle tracker in the region). For sensor 2, the flow is changed in a definitive manner in 50 ms. This time is higher than those defined by the analysis of the velocity and vorticity fields. But here this time is the duration required to reach stabilized flow state. The typical time duration necessary to reattached the airflow along 70% of the chord length can be expressed in non-dimensional form t^+ $\left(t^+ = \frac{tU_0}{0.7\times C}\right)$ in order to compare the present results with the time required to reattach airflow by using other active control systems.

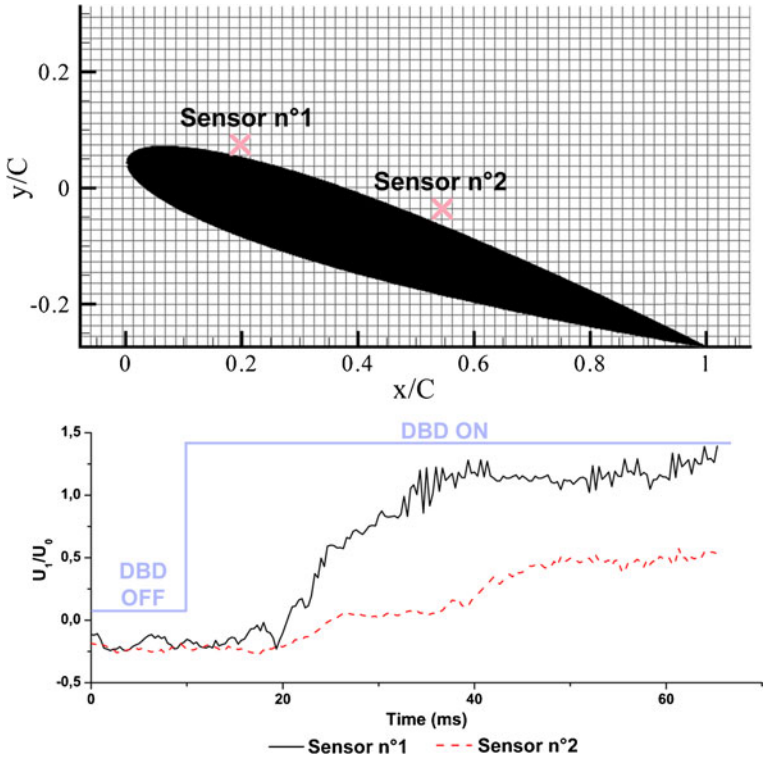

Fig. 26 Time-history of the velocity for three positions along the suction side

Here, the non-dimensional time-scale is about 7. Brzozowski and Glezer observe a characteristic time-scale of about 1.8–2.3 for the flow reattachment along a NACA 4415 in post-stall regime forced by a pulse-combustion actuator [47]. However, a non-dimensional reattachment time of 16 was reported by Darabi and Wygnanski for the forced reattachment by blowing jet along a 2D wing flap at an angle deflection of 23° [43]. These results clearly indicate that the DBD actuator is an effective device to perform rapid lift improvement but a direct comparison to other type of actuator remains complex as it depends on different parameters such as the Reynolds number, the incidence or the physics behind the control process.

4 Conclusion

The present study concerns the control of the airflow over an axisymmetric airfoil in post-stall regime. A single DBD actuator is used to interact with the surrounding airflow ($U_0 = 20$ m/s) with objective to control the separated region above the suction side of a NACA 0015 placed at high angle of attack ($\alpha = 16°$). The time-averaged and time-resolved velocities for post-stalled and reattached flight conditions are measured by a high-speed PIV system. The study is focused on the characterization of the natural and controlled vortex dynamic It is an attempt in improving the understanding of the flow reattachment by highlighting a possible

universal scenario for the flow reattachment process when plasma discharge is used as flow actuator.

A NACA airfoil in stall regime presents a highly dynamic wake flow. Here, the flow separates at the leading edge (x/C = 0.05) and results in a typical separated free shear layer. Formation of discrete coherent structures occurs at x/C = 0.25 and they are shed at a frequency of 90 Hz. When they convect, the flow structures linearly grow along the free shear layer axis and vanish in the wake flow according to two trajectory modes.

Here, continuous actuation promotes a flow reattachment over 70% of the chord length. Transient separation was not observed when the control device operates. However, a new vortex shedding is observed at the separation point moved at x/C = 0.7 due to the discharge. The shedding frequency of the newly formed shear layer is uncorrelated with the actuation as measurements give a value of 100 Hz.

Measurements realized for actuator operating in continuous condition without freestream flow show that the plasma produces a large counter-clockwise vortex. This weak vortical flow structure is formed within 30 ms. This structure is sometime considered as a key factor of the control process for plasma actuation that is not confirmed by the present study. The present investigation suggests that the actuation results in an amplification of a coherent structure with a clockwise sense of rotation. It is not definitively established if the actuation acts on the developing instability or reinforces an already existing flow structure but the increase in coherent structure strength promotes a momentum transfer toward the suction side. A drastic flow topology change is observed and finally the reattachment results from a secondary structure that rolls along the airfoil chord.

In conclusion, the results presented here propose new insights concerning the flow reattached over a NACA 0015 airfoil by performing DBD actuation in continuous mode. As it is widely admitted, flow control strategies based on unsteady actuation are more efficient as they improve the control effects and reduce the consumed power. A similar study has to be performed in a next investigation for periodic excitation by plasma actuation. The separation process could also compose a relevant investigation as well as the detailed study for sufficiently large Reynolds number where plasma actuators fail to produce a significant flow change. By analysing such unfavourable conditions, the conclusions may help to define more effective control approaches.

References

1. Corke, T.C., Post, M.L.: Overview of plasma flow control: concepts, optimization and applications. AIAA paper 2005-563
2. Moreau, E.: Airflow control by non-thermal plasma actuators. J. Phys. D, Appl. Phys. **40**, 605 (2007)
3. Tsubakino, D., Tanaka, Y., Fujii, K.: Effective layout of plasma actuators for a flow separation control on a wing. AIAA paper 2007-474
4. Corke, T.C., Jumper, E.J., Post, M.L., Orlov, D., McLaughlin, T.E.: Applications of weakly-ionized plasmas as wing flow-control devices. AIAA paper 2002–0350
5. Roth, J.R.: Aerodynamic flow acceleration using paraelectric and peristaltic electrohydrodynamic effects of a One Atmosphere Uniform Glow Discharge Plasma. Phys. Plasmas **10**, 2117 (2003)
6. Sosa, R., Moreau, E., Touchard, G., Artana, G.: Stall control at high angle of attack with plasma sheet actuators. Exp. Fluids. **42**, 143 (2007)

7. Göksel, B., Greenblatt, D., Rechenberg, I., Nayeri, C.N., Paschereit, C.O.: Steady and unsteady plasma wall jets for separation and circulation control. AIAA paper 2006-3686
8. Corke, T.C., Mertz, B., Patel, M.P.: Plasma flow control optimized airfoil. AIAA paper 2006-1208
9. Roth, J.R.: Electrohydrodynamically induced airflow in a one atmosphere uniform glow discharge surface plasma. In: 25th IEEE Int. Conf. Plasma Science (1998)
10. Enloe, C.L., McLaughlin, T.E., VanDyken, R.D., Kachner, K.D., Jumper, E.J., Corke, T.C.: Mechanisms and responses of a single dielectric barrier plasma actuator: plasma morphology. AIAA J. **42**, 589 (2004)
11. Pons, J., Moreau, E., Touchard, G.: Asymmetric surface barrier discharge in air at atmospheric pressure: electric properties and induced airflow characteristics. J. Phys. D, Appl. Phys. **38**, 3635 (2005)
12. Boeuf, J.P., Lagmich, Y., Unfer, T.H., Callegari, T.H., Pitchford, L.C.: Electrohydrodynamic force in dielectric barrier discharge plasma actuator. J. Phys. D, Appl. Phys. **40**, 652 (2007)
13. Roth, J.R., Dai, X.: Optimization of the aerodynamic plasma actuator as an EHD electrical device. AIAA paper 2006-1203
14. Forte, M., Jolibois, J., Pons, J., Moreau, E., Touchard, G., Cazalens, M.: Optimization of a dielectric barrier discharge actuator by stationnary and non-stationnary measurements of the induced flow velocity: application to airflow control. Exp. Fluids **43**, 917 (2007)
15. Benard, N., Moreau, E.: Effects of altitude on the electromechanical characteristics of a single dielectric barrier discharge plasma actuator. AIAA paper 2010-4633
16. Benard, N., Balcon, N., Moreau, E.: Electric wind produced by a surface dielectric barrier discharge operating over a wide range of relative humidity. AIAA paper 2009-488
17. Benard, N., Braud, P., Jolibois, J., Moreau, E.: Airflow reattachment along a NACA 0015 airfoil by a surface dielectric barrier discharge actuator—time-resolved particle image velocimetry investigation. AIAA paper 2008-4202
18. Benard, N., Bonnet, J.P., Moreau, E., Griffin, J., Cattafesta, L.N.: Benefits of using hysteresis effects for closed-loop separation control by plasma actuator. AIAA paper 2010-4259
19. Westerweel, J.: Particle image velocimetry—theory and application. Ph.D. thesis, Delft University Press (1993)
20. Bonnet, J.P., Delville, J., Glauser, M.N., Antonia, R.A., Bisset, D.K., et al.: Collaborative testing of eddy structure identification methods in free turbulent shear flows. Exp. Fluids **25**, 97 (1998)
21. Graftieaux, L., Michard, M., Grosjean, N.: Combining PIV, POD and vortex identification algorithms for the study of unsteady turbulent swirling flows. Meas. Sci. Technol. **12**, 1422 (2001)
22. Kerherve, F., Jordan, P., Gervais, Y., Valiere, J.C., Braud, P.: Two-point laser Doppler velocimetry measurements in a Mach 1.2 cold supersonic jet for statistical aeroacoustic source model. Exp. Fluids **37**, 419 (2004)
23. Post, M.L., Corke, T.C.: Separation control using plasma actuators—stationary and oscillating airfoils. AIAA paper 2004-0841
24. Sosa, R., Artana, G.: Steady control of laminar separation over airfoils with plasma sheet actuators. J. Electrost. **64**, 604 (2006)
25. Kitsios, V., Kotapati, R.B., Mittal, R., Ooi, A., Soria, J., You, D.: Numerical simulation of lift enhancement on a NACA 0015 airfoil using ZNMF jets. In: Proceedings of the Center for Turbulence Research Summer Program, pp. 457–468. Stanford University/NASA (2006)
26. Tuck, A., Soria, J.: Micro-jets flow control at the leading edge of a NACA 0015 airfoil. In: Proceeding of 1st Forum in Flow Control (2004)
27. Ben Chiekh, M., Bera, J.C., Sunyach, M.: Synthetic jet control for flows in a diffuser: vectoring, spreading and mixing enhancement. J. Turbul. **4**, 1 (2003)
28. Huerre, P., Monkewitz, P.A.: Local and global instabilities in spatially developing flows. Ann. Rev. Fluid Mech. **22**, 473 (1990)
29. Roshko, A.: On the drag and shedding frequency of two-dimensional bluff bodies. NACA report 3169 (1954)
30. Wu, J.Z., Lu, X.Y., Denny, A.G., Fan, M., Wu, J.M.: Post-stall flow control on an airfoil by local unsteady forcing. J. Fluid Mech. **371**, 21 (1998)
31. Williamson, C.H.K.: Vortex dynamics in the cylinder wake. Ann. Rev. Fluid Mech. **28**, 477 (1996)
32. Artana, G., Sosa, R., Moreau, E., Touchard, G.: Control of the near-wake flow around a circular cylinder with electrohydrodynamic actuators. Exp. Fluids **35**, 580 (2003)
33. Greenblatt, D., Wygnanski, I.J.: The control of flow separation by periodic excitation. Proc. Aerosp. Sci. **36**, 487 (2000)
34. Greenblatt, D., Wygnanski, I.J.: Use of periodic excitation to enhance airfoil performance at low Reynolds numbers. J. Aircr. **38**, 190 (2001)

35. Seifert, A., Greenblatt, D., Wygnanski, I.: Active separation control: an overview of Reynolds and Mach numbers effects. Aerosp. Sci. Technol. **8**, 569 (2004)
36. Mittal, R., Kotapati, R.B., Cattafesta, L.N.: Numericla study of the resonant interactions and flow control in a canonical separated flow. AIAA paper 2005-1261
37. Jukes, T., Choi, K.S., Segawa, T., Yoshida, H.: Jet flow induced by a surface plasma actuator. Proc. Inst. Mech. Eng., Part I, J. Syst. Control Eng. **222**, 347–356 (2008)
38. Balcon, N., Benard, N., Moreau, E.: Formation process of the electric wind produced by a plasma actuator. IEEE Trans. Dielectr. Electr. Insul. **16**, 463–469 (2009)
39. Orlov, D., Apker, T., He, C., Othman, H., Corke, T.C.: Modeling and experiment of leading edge separation control using SDBD plasma actuators. AIAA paper 2007-0877
40. Benard, N., Moreau, E.: Capabilities of the dielectric barrier discharge plasma actuator for multi-frequency excitations. J. Phys. D, Appl. Phys. **43** 145201
41. Benard, N., Jolibois, J., Moreau, E.: Lift and drag performances of an axisymmetric airfoil controlled by plasma actuator. J. Electrost. **67**, 133–139 (2009)
42. Zaman, K.B.M.Q., McKinzie, D.J., Rumsey, C.L.: A natural low-frequency oscillation of flow over an airfoil near stalling conditions. J. Fluid Mech. **202**, 403 (1989)
43. Darabi, A., Wygnanski, I.: Active management of naturally separated flow over a solid surface. Part 1. The forced reattachment process. J. Fluid Mech. **510**, 105 (2004)
44. Gillaranz, J.L., Traub, L.W., Rediniotis, O.K.: Characterization of a compact, high power synthetic jet actuator for flow separation control. AIAA paper 2002-0127
45. Duvigneau, R., Visonneau, M.: Simulation and optimization of stall control for an airfoil with synthetic jet. Aerosp. Sci. Tech. **10**, 279 (2006)
46. Tuck, A., Soria, J.: Active flow control over a NACA 0015 airfoil using a ZNMF jet. In: Proceeding of the 15th Australian Fluid Mechanics Conference, 13–17 December, Sydney, Australia (2004)
47. Brzozowski, D., Glezer, A.: Transient separation control using pulse-combustion actuator. AIAA paper 2006-3024